

Supplementary Materials for **Toughness of carbon nanotubes conforms to classic fracture mechanics**

Lin Yang, Israel Greenfeld, H. Daniel Wagner

Published 5 February 2016, *Sci. Adv.* **2**, e1500969 (2016)

DOI: 10.1126/sciadv.1500969

This PDF file includes:

Note S1. Molecular dynamics.
Note S2. Bond failure criterion.
Note S3. Defect-free SWNT under tension.
Note S4. SWNT with defects under tension.
Note S5. Effect of prestresses in topological defects.
Note S6. Comparison with solid mechanics theories.
Note S7. Alternative estimation of the SWNT fracture toughness.
Table S1. Defect dimensions and simulation results.
Fig. S1. Simulated stresses around a Stone-Wales defect.
References (54–61)

Other Supplementary Material for this manuscript includes the following:
(available at advances.sciencemag.org/cgi/content/full/2/2/e1500969/DC1)

Movie S1. Crack propagation illustration (separate file).

Supplementary Materials

Note S1. Molecular dynamics (MD)

Many attempts have been made to study the stress-strain properties of CNTs (7-9, 16-21). Among them, the MD method is often used because it provides atomic-level resolution of the mechanical properties, including dynamic behavior and equilibrium properties of the nanomaterial ensemble (54). Specifically to our study, the atomic-level resolution allows us to accurately simulate point defects in a variety of shapes and sizes. We use in the present work the LAMMPS MD simulator (48) with the COMPASS force field (49).

Several MD studies simulate tensile loading of defect-free CNTs, and calculate the stress-strain curves by using the Tersoff-Brenner (TB) reactive empirical bond-order (REBO) potential (16-21). In such simulations, CNTs do not fracture in a brittle manner, rather they do so plastically and bonds can be reformed during deformation. These simulations predict that the plastic fracture occurs at a tensile strain above 20%, without any bond rupture below it (16-21), in contrast to experimental evidence (7-11). The precision of this method is not sufficient for the purpose of simulating the potential variations arising from small elastic deformations (55-58), or the onset of bond interaction distance cut-off (about 2Å) (16), and therefore it is not suitable for predicting the fracture behavior of a defective SWNT at room temperature.

Hence, in the current study, we chose to use the COMPASS force field, which has been proven to accurately describe the mechanical properties of CNTs (50-51). COMPASS is an *ab initio* force field that has been parameterized and validated using condensed-phase properties (49), and is widely used by the Materials Studio software from Accelrys. Compared with other force fields, its bonded potential energy (the energy associated with chemical bonds) includes high-order (cubic and quadratic) bond, bond angle, torsion angle (dihedral), and out-of-plane angle (improper torsion) terms, as well as cross-coupling terms between them (49). The axial tension on the SWNT sp² bonded hexagonal network would indeed cause such diverse molecular structural changes, accounted for by the force field, enabling accurate prediction of the CNT structural deformation.

Note S2. Bond failure criterion

The comprehensive force field characteristics allow us to use as a bond failure criterion the bond dissociation energy, the amount of energy required to break a covalent carbon-carbon bond. The simulated bonded energy can be evaluated against the bond dissociation energy in order to detect a bond failure. The tensile force on each atom can be computed by using a symmetric per-atom stress tensor (27, 50-51), enabling us to depict an atomic-resolution color map of force distribution throughout the SWNT. The resulting tensile force reflects the magnitude of the bonded potential energy along the tensile direction (27).

In our current simulation, we use the maximum allowed bond force, derived from the bond dissociation energy, to detect when the bond force exceeds the bond breaking strength. The covalent bond between carbon atoms breaks at a force of about 10 nN (28), corresponding to a tensile stress of about 200 GPa. In using this criterion, we can detect local bond breakage at the defect tip, determine the SWNT tensile stress at that instance, and trace the crack growth until rupture. Furthermore, this criterion enables us to evaluate the criticality of a particular shape and size of a vacancy or a Stone-Wales defect. This maximum bond force criterion is similar to the maximum stress criterion used for brittle macro-materials in fracture mechanics (59).

Note S3. Defect-free SWNT under tension

To obtain a reference value for the strength of a defect-free tube (i.e., the ideal strength), and to assert the validity of our model, we first simulated tensile loading of defect-free tubes, up to a maximum strain of 20%. The corresponding stress-strain curves are plotted in Fig. 2A in the main text. Both stress-strain curves are nearly linear, in contrast with the nonlinear curves obtained by a Tersoff-Brenner (TB) potential (16, 18-21). The calculated Young's modulus is 1 TPa for the zigzag tube and 0.88 TPa for the armchair tube, in agreement with the literature (1-3). The reason for the difference in modulus between armchair and zigzag tubes is that a third of the carbon-carbon bonds in the zigzag tube are oriented in the axial direction, whereas no such orientation is present in the armchair tube. A small stress bias is observed at zero strain, attributed to initial strains induced by the tube curvature. This bias is negligible in view of the low bending rigidity of graphene (60), and is not present in similar simulations of graphene.

Assuming the maximum tensile strain of a defect-free SWNT is 20%, as predicted theoretically (4-5), the resulting tensile strengths are about 175 and 200 GPa for the armchair and zigzag tubes, respectively. The corresponding tensile force acting on the atoms is approximately 10 nN, comparable to the bond breaking strength (28). These values confirm that our model is in agreement with theoretical predictions for defect-free SWNTs, as presented in the introduction.

Under loading, the carbon-carbon bonds parallel to the tube axis are elongated and the bond angles between them are enlarged, whereas bonds perpendicular to the tube axis experience slight shortening (Fig. 2A in the main text). The periodical undulation in the stress-strain curves is likely the result of elastic waves that propagate along the SWNT axis and bounce back from its ends, yet its magnitude can be viewed as a low noise. The tensile forces acting on the atoms are distributed almost evenly throughout the tube in both tube configurations.

Note S4. SWNT with defects under tension

Table S1 summarizes the defects types and dimensions used in the simulation, and the simulation results for strength, stress concentration, and fracture toughness.

Table S1. Defect dimensions and simulation results.

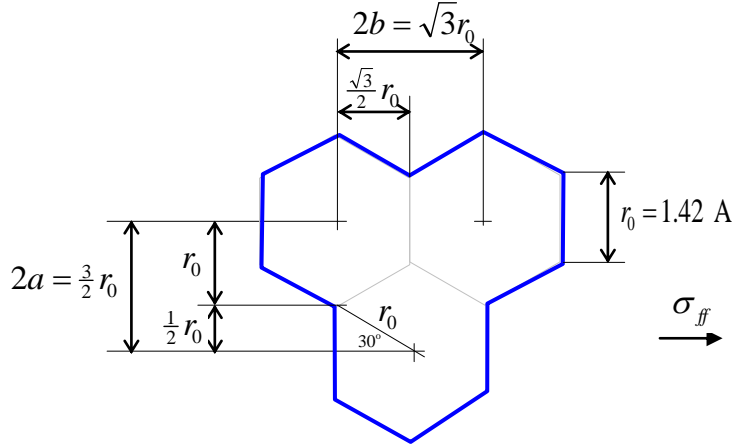
Defects			Defects dimensions				Strength and toughness simulation results				
CNT chirality	Defect Type	Missing atoms	$2a$	$2b$	$\frac{a}{r_0}$	$\frac{2a}{\pi D}$	σ_f	σ_f	K_t	K_t	K_{Ic}
			Å	Å			GPa	nominal GPa		nominal	Mpa m ^{0.5}
Armchair	(a)	SW					172.2		1.02		
	(b)	1	2.13	2.46	0.75	0.05	140.0	147.4	1.25	1.19	2.70
	(c)	2	4.26	2.46	1.50	0.10	94.50	105.0	1.85	1.67	2.72
	(d)	2	2.13	3.69	0.75	0.05	119.0	125.3	1.47	1.40	2.29
	(e)	2	4.26	4.92	1.50	0.10	85.4	94.9	2.05	1.84	2.45
	(f)	3	4.26	6.15	1.50	0.10	82.6	91.8	2.12	1.91	2.37
	(g)	3	2.13	4.92	0.75	0.05	130.7	137.6	1.34	1.27	2.52
	(h)	3	4.26	3.69	1.50	0.10	84.0	93.3	2.08	1.87	2.41
	(i)	3	6.39	2.46	2.25	0.15	69.3	81.5	2.53	2.15	2.58
Zigzag	(a)	SW					123.0		1.63		
	(b)	1	2.46	2.13	0.87	0.06	166.7	177.1	1.20	1.13	3.48
	(c)	2	2.46	4.26	0.87	0.06	120.0	127.5	1.67	1.57	2.51
	(d)	2	3.69	2.13	1.30	0.09	120.7	132.4	1.66	1.51	3.19
	(e)	2	2.46	4.26	0.87	0.06	146.7	155.9	1.36	1.28	3.06
	(f)	3	3.69	4.26	1.30	0.09	104.0	114.1	1.92	1.75	2.75
	(g)	3	2.46	6.39	0.87	0.06	121.3	128.9	1.65	1.55	2.53
	(h)	3	6.15	4.26	2.16	0.15	73.3	85.9	2.73	2.33	2.67
	(i)	3	4.92	2.13	1.73	0.12	87.0	98.6	2.30	2.03	2.74

Table legend:

The defect types are illustrated in Fig. 1 in the main text.

SW stands for Stone-Wales defect.

$2a$ and $2b$ are the defect length (perpendicular to the tube axis) and width, calculated as shown in the following monovacancy example:



a / r_0 is the ratio of the defect semi-length to the C=C bond length.

$2a / (\pi D)$ is the ratio of the defect semi-length to the tube perimeter.

σ_f is the tube strength. The nominal value (used in Fig. 4B in the main text) is obtained by dividing by $1 - 2a / (\pi D)$.

K_t is the maximum stress concentration. The nominal value (used in Fig. 4A in the main text) is obtained by multiplying by $1 - 2a / (\pi D)$.

$K_{Ic} = \sigma_f \sqrt{\pi a}$ is the CNT fracture toughness (using the nominal σ_f).

Note S5. Effect of prestresses in topological defects

It is generally assumed that Stone-Wales defects are not very harmful, as their structure has no missing atoms and does not diverge much from the regular hexagonal network. The simulated Stone-Wales defect in an armchair SWNT indeed supports this assumption, as it yields a strength close to that of a defect-free SWNT, but, the same defect in a zigzag SWNT (rotated 90°) exhibits a significant strength reduction (~40%). Interestingly, intuition would imply the opposite, namely that when the defect's longer axis is perpendicular to the tube axis, the defect should be more harmful than when it is parallel. The reason for this peculiar behavior is the topological deviation from the regular hexagonal network, induced by atomic rearrangement (coupling of two pentagons and two heptagons). This conformation introduces inherent prestresses in the absence of external loading (Fig. S1A,B), as well as high local stiffness as a result of bond rotation. The rotated central bond in this structure causes some of the bonds on the defect perimeter and close vicinity to extend and some to contract, resulting in respective tension and compression forces. This phenomenon is not observed in vacancy defects, as the hexagonal structure around such defects is nearly unperturbed.

Specifically, as shown by the simulation, the stress profile around a Stone-Wales defect includes tension forces in the direction of the defect's long axis up to a maximum of about 2.1 nN, and compression stresses in the direction of the defect's short axis up to a maximum of about -6 nN. When the tension prestress aligns with the direction of the applied load, as is the case with the defect in the zigzag SWNT, the stress induced by the load is superimposed on the prestress, and the highly stressed bonds (red atoms in Fig. S1A) break earlier. By contrast, when the tension prestress is perpendicular to the direction of the load, as is the case with the defect in the armchair SWNT, it does not contribute to the local stress in the direction of the load (Fig. S1B), and therefore the tube strength is not harmed.

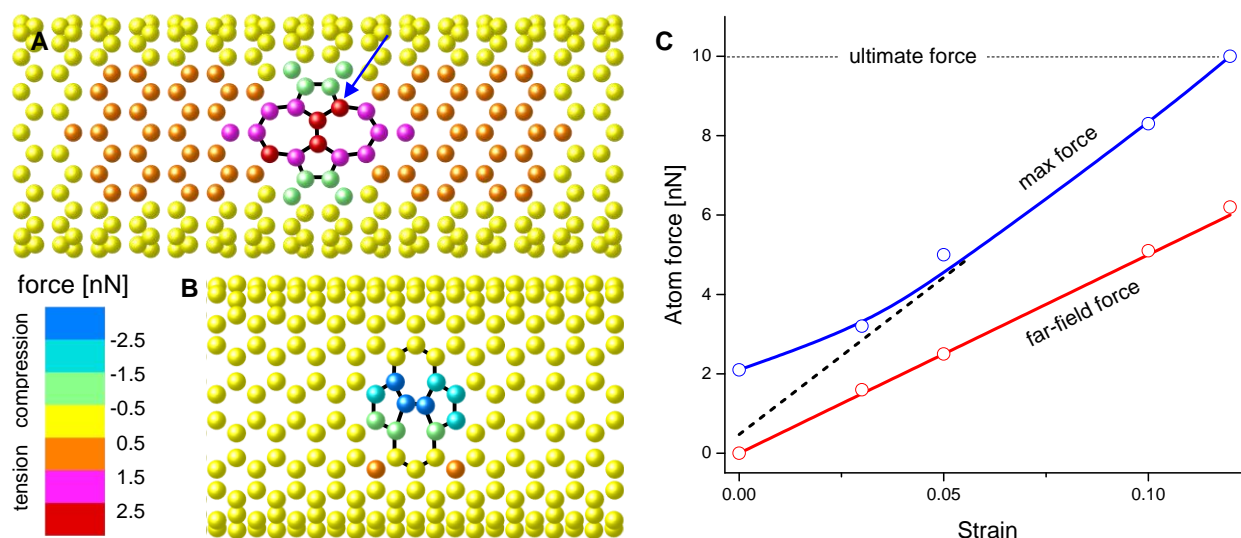


Fig. S1. Simulated stresses around a Stone-Wales defect. (A) Tension prestresses in a zigzag SWNT at zero strain, expressed in terms of atom forces in the axial (horizontal) direction. (B) Compression prestresses in the axial direction in an armchair SWNT at zero strain. (C) Maximum atom force (at the atom marked by arrow in a) and far-field atom force versus tube strain. The maximum force asymptote is depicted by a dashed line.

The stress-strain plot in Fig. S1C provides further insight into this effect. While the far-field force increases linearly with the strain, as expected, the maximum force at the defect boundary starts with a bias of the magnitude of the tensile prestress, then rises moderately with the strain up to a strain of about 5%, and eventually rises with a higher slope until reaching the ultimate force. The steeper slope during high strains indicates that, in addition to the contribution of the prestress to the overall force, there is inherent stress concentration in the structure, which can be estimated as ~ 1.6 by comparing the maximum and far-field slopes.

Note S6. Comparison with solid mechanics theories

The applicability of classic macroscale theories to nanoscale is often debated in the literature, specifically the limit size below which macroscale theories fail to predict the behavior of nanomaterials. The various defect types and orientations simulated in the present study provide a good opportunity to examine the applicability of concepts from solid mechanics theories to nanomaterials such as CNTs, particularly so since experimental evaluation of the harm caused by different defect types is not practical.

To that end, we compare the simulation results to predictions from the classic solid continuum theories of linear elasticity (LE) and linear elastic fracture mechanics (LEFM), and to predictions from the more recent theory of quantum fracture mechanics (QFM). The compared mechanical properties are the maximum stress concentration factor, $K_t = \sigma_{\max} / \sigma_{ff}$ (σ_{\max} is the maximum local stress and σ_{ff} is the far-field loading stress, defined in Fig. 1A in the main text), and the relative fracture strength, σ_f / σ^* (σ_f is the tube fracture strength and σ^* is the strength of a defect-free tube). Stone-Wales defects are not included in this analysis, since they involve nonzero stresses at zero load (see the discussion in Supplementary note S5), and therefore their analysis is deferred to future research.

Initially, based on continuum solid mechanics, we expect the variations in stress concentration and strength to be dependent on the defect dimensions, namely its length $2a$ (orthogonal to the tube axis) and width $2b$ (parallel to the tube axis), or its self-similar shape a/b . Note that $2a$ and $2b$ are defined as the distances between the centers of the defect's extreme hexagonal cells (see drawings in Figs. 4A and 5B in the main text), rather than the edges of the cells, so that when $2a$ and $2b$ are zero the shape converges to a regular hexagonal cell (that is, no defect is present). Furthermore, we expect dependence on the curvature radius ρ at the defect tip, as well as on the defect orientation with respect to the tube's main axis.

However, such dependencies were not observed in the simulated SWNTs. Statistical correlation analysis, using the simulated stress concentration and strength results of all the vacancy defects under study (Fig. 1B,C in the main text), shows that indeed both K_t and σ_f/σ^* are strongly dependent on the defect length $2a$ ($\text{corr}(K_t, a) \cong 0.96$ and $\text{corr}(\sigma_f/\sigma^*, a) \cong -0.92$). However, K_t and σ_f/σ^* are seen to be weakly dependent on the defect width $2b$ ($\text{corr}(K_t, b) \cong 0.26$ and $\text{corr}(\sigma_f/\sigma^*, b) \cong -0.40$) as well as on the aspect ratio a/b , the curvature and the orientation.

In other words, the mechanical properties of the defective SWNTs are dominated by the defect length perpendicular to the tube axis, whereas the effects of the defect shape and orientation are secondary. This surprising result is demonstrated in Fig. 4 in the main text, where K_t and σ_f/σ^* are depicted against a , normalized by the constant bond length r_0 . The general behavior is similar for both tube chiralities (marked by filled and unfilled symbols for armchair and zigzag tubes, respectively).

Note S7. Alternative estimation of the SWNT fracture toughness

The LEFM stability condition for brittle materials leads to $K_{Ic} = \sqrt{2E\gamma}$ (plane stress), where E is the elastic modulus of the tube and γ is the energy required to create the two new crack surfaces (i.e., the energy to break bonds) (30-32, 61). The energy to break a single C=C bond is of the order of $U_{c=c} \cong 1.7$ eV, estimated from the formation energy of a 2-atom vacancy (8.5 eV / 5 bonds) (36). Using the crack growth resulting from a single bond breakage ($\delta a = \sqrt{3}r_0 \cong 2.46$ Å where $r_0 = 1.42$ Å) and the SWNT layer thickness ($t = 3.4$ Å) to estimate the area of the two new surfaces created by removing a single bond, we calculate the surface energy $\gamma \cong U_{c=c} / (t\delta a) \cong 3.3$ Jm⁻². Substituting the simulated moduli $E = 1$ TPa for the zigzag tube and $E = 0.88$ TPa for the armchair tube, we obtain $K_{Ic} \cong 2.4$ MPa m^{0.5} for the armchair tube and $K_{Ic} \cong 2.6$ MPa m^{0.5} for the zigzag tube, close to the values obtained from the simulation.